MATERIALS SCIENCE

Switching it up: New mechanisms revealed in wurtzite-type ferroelectrics

Cheng-Wei Lee[1]*, Keisuke Yazawa[1,2], Andriy Zakutayev[2], Geoff L. Brennecka[1], Prashun Gorai[1,2]*

Wurtzite-type ferroelectrics have drawn increasing attention due to the promise of better performance and integration than traditional oxide ferroelectrics with semiconductors such as Si, SiC, and III-V compounds. However, wurtzite-type ferroelectrics generally require enormous electric fields, approaching breakdown, to reverse their polarization. The underlying switching mechanism(s), especially for multinary compounds and alloys, remains elusive. Here, we examine the switching behaviors in $Al_{1-x}Sc_xN$ alloys and wurtzite-type multinary candidate compounds we recently computationally identified. We find that switching in these tetrahedrally coordinated materials proceeds via a variety of nonpolar intermediate structures and that switching barriers are dominated by the more-electronegative cations. For $Al_{1-x}Sc_xN$ alloys, we find that the switching pathway changes from a collective mechanism to a lower-barrier mechanism enabled by inversion of individual tetrahedra with increased Sc composition. Our findings provide insights for future engineering and realization of wurtzite-type materials and open a door to understanding domain motion.

INTRODUCTION

Ferroelectrics are polar materials whose spontaneous polarization can be reoriented via an external electric field. This phenomenon enables the poling of polycrystalline piezoelectrics and has found direct application from non-volatile memory and sensors to energy harvesting and storage (*1*–*3*). Recently, as first demonstrated in $Al_{1-x}Sc_xN$ by Fichtner *et al.* in 2019 (*4*), wurtzite-type ferroelectrics have drawn rapid interest from academia and industry due to their high spontaneous polarization [e.g., >100 μC/cm^2 for nitrides (*5*)] and the potential for direct integration with existing semiconductors such as Si, GaN, and SiC (*3*, *6*). One major challenge for all currently known wurtzite-type ferroelectrics [$Al_{1-x}Sc_xN$ (*4*), $Ga_{1-x}Sc_xN$ (*7*), $Al_{1-x}B_xN$ (*8*), $Al_{1-x}Y_xN$ (*9*), and $Zn_{1-x}Mg_xO$ (*10*) alloys] is that the coercive field, E_c, required to switch the polarization is several megavolts per centimeter, which is dangerously close to the maximum breakdown fields of these same materials and is roughly one to two orders of magnitude larger than more common perovskite ferroelectrics (*4*, *11*).

To address this challenge and reduce E_c, there are generally two approaches. One is to further engineer known wurtzite materials like AlN and ZnO via alloying and straining (*4*, *7*, *8*, *10*, *12*), while the other is to explore and develop new wurtzite(-type) materials that have lower coercive fields (*11*, *13*, *14*). Ultimately, the goal is to identify the underlying polarization switching mechanisms and the structure-property relationships that control E_c; in other words, what deviations from the baseline wurtzite structure are involved in the transition from a positive-polarity wurtzite (wz^+) to the equivalent negative-polarity wurtzite (wz^-)? We want to emphasize that the present study focuses on favorable pathways for polarization inversion and, therefore, represents possible atomic configurations that could be mapped to static domain walls. No attempt is made in the current work to describe the motion of these walls that would correspond to macroscopic ferroelectric switching.

The simplest model of this process, and the one proposed in the original Fichtner *et al.* work (*4*), essentially involves the cation and anion sublattices collectively squeezing "through" one another via a nonpolar hexagonal structure ($wz^+ \rightarrow h^0 \rightarrow wz^-$, see collective mechanism in Fig. 1B). This pathway was proposed in 2016 as part of a study that identified the hexagonal intermediate structure as the "proper" nonpolar reference structure for calculating wurtzite polarity (*15*). Earlier work investigated a pathway via the nonpolar zincblende structure ($wz^+ \rightarrow zb^0 \rightarrow wz^-$) (*16*, *17*); while using the nonpolar zincblende structure as the computational reference structure leads to spontaneous polarization values that are one to two orders of magnitude too small (*5*), this does not preclude such a dislocation-mediated process from occurring during polarization inversion. Along similar lines, inversion domain boundaries in as-grown III-N films have been extensively studied for many years and provide an important example of one possible intermediate state between fully wz^+ and wz^- structures (*18*–*20*).

Three groups have recently and independently contributed strong evidence that the simple $wz^+ \rightarrow h^0 \rightarrow wz^-$ pathway is likely not the complete story for ferroelectric wurtzites. The Kiel group directly imaged via transmission electron microscopy (TEM) a laterally extended inversion boundary (*21*). A computational study from Liu *et al.* (*22*) identified a nonpolar structure that resembles β-BeO, and Calderon *et al.* (*23*) imaged dynamic inversion via TEM and matched the atomic structure to that of previously known inversion domain boundaries. In our recent computational search for multinary wurtzite-type ferroelectrics with reduced switching barriers and larger breakdown fields (*14*), we found that most of the studied compounds follow switching pathways that pass through nonpolar structures (see individual mechanism in Fig. 1B). Together, these findings indicate greater complexities than what is captured in the simple $wz^+ \rightarrow h^0 \rightarrow wz^-$ pathway and highlight the importance of the local atomic environment in polarization inversion. By extension, chemical diversity may induce different switching pathways, though the underlying mechanisms remain elusive.

To address this, we perform a systematic study on (i) switching pathways for different Sc compositions ($x < 0.44$) in $Al_{1-x}Sc_xN$ alloys, and (ii) the switching pathways for all of the candidate compounds in our previous computational search (*14*). Figure 1 shows the schematic energy landscape and switching sequence of the newly revealed individual switching mechanism for multinary compounds and alloys. The collective $wz^+ \rightarrow h^0 \rightarrow wz^-$ switching pathway has a

[1]Colorado School of Mines, Golden, CO 80401, USA. [2]National Renewable Energy Laboratory, Golden, CO 80401, USA.
*Corresponding author. Email: clee2@mines.edu (C.-W.L.); pgorai@mines.edu (P.G.)

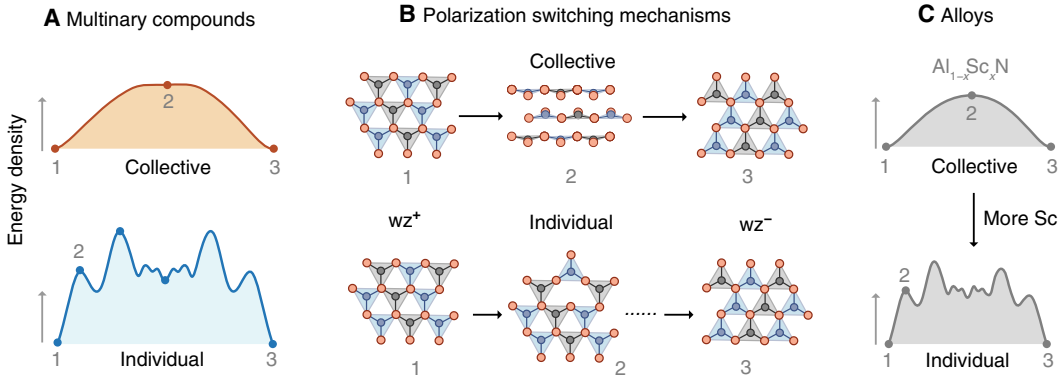

Fig. 1. New polarization switching mechanisms in multinary compounds and alloys. (**A**) The polarization switching in few multinary (beyond binary) compounds (1→2→3) is characterized by a simple energy density landscape, and proceeds via a layered hexagonal structure, labeled "Collective" in (**B**). In contrast, many multinary compounds undergo more complex polarization switching through unique half-switched nonpolar structures, labeled "Individual," characterized by sequential switching of cation tetrahedra. (**C**) $Al_{1-x}Sc_xN$ alloys exhibit a change from collective to individual mechanism with increasing Sc content.

smoother energy landscape, while the landscape for the individual pathway is more complicated and has multiple local minima. Figure 1B further shows the corresponding atomic configurations, highlighting that the individual pathways are so named due to the sequential switching of individual cation tetrahedra. We find that increasing Sc content in the $Al_{1-x}Sc_xN$ alloy not only reduces the switching barrier but also promotes individual switching, as schematically shown in Fig. 1C. Across the 22 investigated compounds that exhibit individual switching, we find that five distinct nonpolar structures—including the recently reported β-BeO–like structure—show distinctive repeating patterns associated with the chemical stoichiometries of the material. Last, we find that the switching barriers in multinary wurtzite-type compounds are dominated by the cations with higher electronegativity. Overall, our findings provide critical insights into the polarization inversion of wurtzite-type ferroelectrics.

RESULTS

Switching pathways in $Al_{1-x}Sc_xN$ alloys

To date, all demonstrations of ferroelectricity in wurtzite-based materials have been in AlN or in chemically disordered alloys (*4*, *7*–*10*). Despite emerging experimental and theoretical evidence (*21*–*23*), a systematic understanding of the atomic-scale switching pathways in these alloys remains unclear. To gain insights into the switching mechanism and the effect of Sc addition to AlN, we calculate the minimum energy pathways (MEPs) of $Al_{1-x}Sc_xN$ alloys using the solid-state nudged elastic band (SS-NEB) method, between its positive-polarity and negative-polarity structures. We perform a systematic study of the polarization switching pathways and barriers for $Al_{1-x}Sc_xN$ alloys, with Sc composition x of 0.055, 0.22, 0.28, 0.305, 0.36, and 0.44. The largest x is chosen based on the highest reported experimental value (*4*, *24*) and predicted the stability range of the wurtzite-type structure (*25*, *26*) in this alloy. For each x, we investigate four alloy models with different random distributions of Sc and apply the SS-NEB method to determine the pathways and barriers (see Materials and Methods for details). We use four alloy models at each composition to build statistics of the switching pathways and barriers; the statistics capture the different local environments in the alloy.

Figure 2A shows the predicted spontaneous polarization (P_s) for $Al_{1-x}Sc_xN$ alloys. We find that P_s decreases with increasing x and the trend is consistent with experimental observations (Fig. 2B). Overall, the predicted values are slightly higher than the reported experimental values, but this is expected because of temperature effects (*27*, *28*) that are not included in the calculations.

The commonly assumed switching mechanism for pure wurtzite AlN is the $wz^+ \rightarrow h^0 \rightarrow wz^-$ switching pathway (collective mechanism in Fig. 1B) (*4*, *5*), and this is consistent with our SS-NEB calculations. With increasing x, we find that $Al_{1-x}Sc_xN$ alloys follow the same collective switching pathway up to $x = 0.22$. The switching proceeds via the fivefold coordinated h-BN–like structure. At around $x = 0.28$, we find that some of the four alloy models follow individual switching pathways (Fig. 2C). For $x \geq 0.36$, all four alloy models we study show an individual switching mechanism. Such predicted behavior suggests that alloying with Sc in high concentration promotes individual switching for wurtzite-type $Al_{1-x}Sc_xN$ alloys.

Next, we take a deeper look into the individual switching pathway and use one of the $Al_{0.64}Sc_{0.36}N$ alloy models as an illustrative example (Fig. 2C). The switching barrier is defined by the largest barrier between a valley and its neighboring peak toward the switching direction (ω_s in Fig. 2C). We find that the energy landscape along the MEP for alloys that exhibit individual switching is asymmetric and has more peaks and valleys. This asymmetry arises from differences in local environment, i.e., first nearest neighbors of cations, because of the disordered nature of the alloys. We also track the number of tetrahedra with flipped polarization at each local minimum along the switching pathway and find that multiple tetrahedra can flip at the same time, and the number generally increases along the pathway (i.e., as the overall fraction of switched tetrahedra increases).

In general, we find that the overall switching barrier decreases linearly with increasing x (Fig. 2D). Because switching barrier is, to a first-order approximation, proportional to the coercive field (E_c), our results are consistent with the seminal experimental work by Fichtner *et al.* (*4*) (Fig. 2B) and all subsequent reports (*12*, *29*, *30*), in which E_c was shown to decrease linearly with Sc composition. In addition, such agreement between experiment and computational results supports the common assumption that switching barriers calculated by the SS-NEB method can represent the relative tendency to switch (*11*, *31*, *32*).

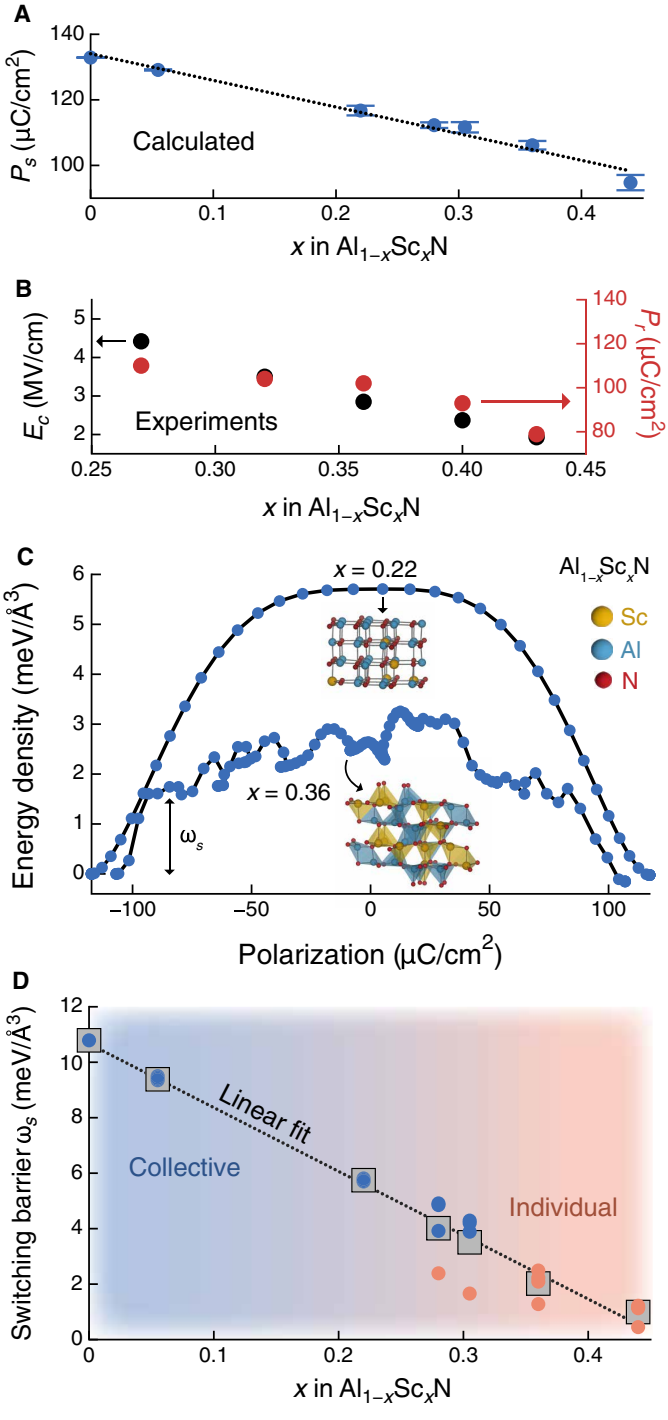

Fig. 2. Switching mechanism in $Al_{1-x}Sc_xN$. (**A**) Calculated spontaneous polarization of $Al_{1-x}Sc_xN$ as a function of x. Error bars are SD across four structures. (**B**) Experimentally measured coercive field (E_c) and remnant polarization (P_r) from (*4*) for comparison. These thin-film samples have residual stress <0.2 GPa. (**C**) Switching pathway of $Al_{0.78}Sc_{0.22}N$ (Collective) and $Al_{0.64}Sc_{0.36}N$ (Individual). (**D**) Predicted switching barrier (ω_s) of $Al_{1-x}Sc_xN$ as a function of x. Squares are average over four structures. Blue and orange circles are individual data points for collective and individual switching, respectively.

For compositions where a mix of switching mechanism is observed across the four alloy models ($x = 0.28$ and 0.305), the switching barriers differ notably between individual (orange circles) and collective (blue circles) switching. At a given x, we find that the barriers of individual switching are always smaller than the ones of collective switching. This showcases the importance of identifying the new switching pathway because the commonly assumed $wz^+ \rightarrow h^0 \rightarrow wz^-$ pathway (collective mechanism) leads to higher predicted barriers for $Al_{1-x}Sc_xN$ alloys with high x.

An important consequence of this proposed transition from collective to individual switching is that it represents an additional mechanism for the reduction in coercive field. Figure 2D highlights the linear relationship associated with the average switching barrier across our limited test cases, but we note that the lowest barrier available under a homogeneous field should dominate experimental results on real materials. Experimental reports of the Sc dependence of E_c include a great deal of scatter, and reports for $x < 0.2$ are particularly sparse. Thus, a careful and systematic study of the relationship between x and E_c in nominally identical $Al_{1-x}Sc_xN$ samples would be valuable for (in)validating the mechanistic transition proposed here. On the basis of our calculations, there should be an inflection point in the switching barrier versus x (fig. S4) due to the change in the dominant mechanism but is not resolvable within the SD across the four models.

Our results also point to a correlation between chemical complexity and switching mechanism. With increasing Sc content, the $Al_{1-x}Sc_xN$ alloy departs from the collective mechanism that is observed in pure AlN to the individual mechanism, which is possibly triggered by larger local distortions produced by Sc. To better understand this correlation, we turn to multinary compounds where the additional effects of site disorder are absent. We first revisit the commonly assumed pathway for wurtzite-type materials and then present an in-depth analysis of individual switching mechanism in multinary compounds.

Commonly assumed switching pathway in compounds

Early work on calculating the spontaneous polarization of wurtzite compounds, in particular GaN, assumed a zincblende nonpolar structure as the reference phase (*16*, *33*). Those studies treated the zincblende structure as a natural choice for the nonpolar structure, but did not probe the switching pathways because wurtzite compounds were not thought to be strong candidates for ferroelectricity. In the early 2000s, Takeuchi (*34*) predicted the existence of a (meta) stable layered hexagonal phase ($P6_3/mmc$) of ScN. Farrer and Bellaiche confirmed the metastability of the hexagonal ScN phase. More than a decade later, ferroelectricity in wurtzite oxides and chalcogenides was computationally predicted (*15*, *35*); in these studies, it was assumed that the polarization switching would proceed through nonpolar, hexagonal BN–like phases akin to the hexagonal ScN, whose metastability was proposed earlier. Recent studies have assumed the simple wurtzite-hexagonal-wurtzite switching pathway because of the trivial phase transformation from wurtzite to the hexagonal phase. Using SS-NEB calculations, we confirm that in binary and a few ternary wurtzite-type compounds, this commonly assumed transformation is indeed the switching pathway in these materials.

Using Mg_3MoN_4 as an example, Fig. 3 shows the collective switching pathway in a multinary compound. Mg_3MoN_4 has the space group of $Pmn2_1$ (*31*), which belongs to a subgroup of the wurtzite space group $P6_3mc$ (*36*). The structure labeled 1 in Fig. 3 is the positive-polarity

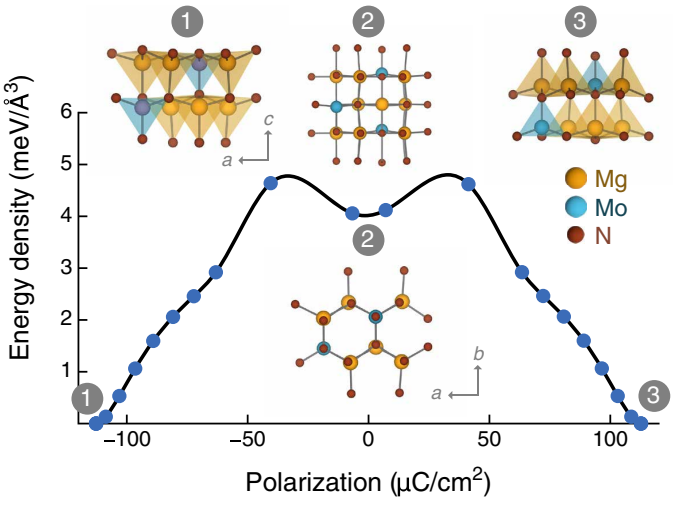

Fig. 3. Collective switching in multinary compounds. Polarization switching in Mg_3MoN_4 proceeds via the collective mechanism. Structures (1), (2), and (3) represent positive polarity, nonpolar structure, and negative polarity. Nonpolar structure (2) is a layered hexagonal phase; views along the *b* and *c* axes are presented. The crystallographic axes are such that the cation tetrahedra are pointed along the *c* axis.

structure, which closely resembles the wurtzite structure except for local distortions and two different cations (Mg, Mo). Such a structure is commonly referred to as a wurtzite-type structure. As Mg_3MoN_4 transforms to a nonpolar structure (structure 2 in Fig. 3), its structure becomes fivefold coordinated and resembles a planar hexagonal phase; it is thus commonly referred to as a hexagonal structure. After complete polarization inversion, Mg_3MoN_4 exhibits the negative-polarity structure that has the same wurtzite-type structure as the positive-polarity structure but with polarization pointing in the opposite direction.

Prior reports on binary compounds have reported that the nonpolar intermediate structure represents a saddle point in the MEP (*11*, *13*, *23*). We find that multinary compounds that follow the comparable wurtzite-hexagonal-wurtzite pathway can have a shallow local minimum at or near the nonpolar intermediate structure rather than it being a saddle point. This indicates that the nonpolar structure (or slight deviations from it) can be metastable without spontaneous relaxation to either polarity of wurtzite structure. Such shallow local minima have also been reported for $ZnTiN_2$ (*14*), $ZnZrN_2$ (*37*), Mg_3WN_4, (*38*), and $Al_{1-x}Sc_xN$ alloys (*22*).

The energy along the wurtzite-hexagonal-wurtzite transformation pathway, i.e., static total energies of linearly interpolated structures between positive-polarity and negative-polarity structures, is commonly used to qualitatively estimate the switching barrier for binary wurtzite materials (*11*, *35*). Our results suggest that the energy difference between the wurtzite-type and hexagonal structures can also be a good predictor of switching barrier for multinary wurtzite-type materials that follow this pathway.

However, a majority of the studied multinary compounds (>90%) in our recent computational search (*14*) exhibit switching pathways via different nonpolar structures, and the predicted switching barriers are lower than the barriers associated with their wurtzite-hexagonal-wurtzite pathway counterparts. These findings are consistent with the most recent computational and experimental works on $Al_{1-x}B_xN$ alloys, which also identified a similar nonpolar structure (*22*, *23*). Together, these findings strongly suggest that the atomic-scale switching mechanisms are far more complex than initially hypothesized and necessitate further investigations for alloys and multinary compounds.

Switching pathways in compounds

In comparison to the collective mechanism discussed above, Fig. 4 showcases one of the recently identified switching pathways in a multinary compound. We use $MgSiN_2$ as an example because it is one of the top candidates from our previous computational search (*14*). Comparing it to the pathway of Mg_3MoN_4, we find that $MgSiN_2$ has more peaks along the switching pathway and the local minima are deeper in energy. Furthermore, when we associate these peaks with the underlying atomic motions, we find that, instead of collective and homogeneous distortion and inversion as shown for Mg_3MoN_4 and other systems following the wurtzite-hexagonal-wurtzite switching pathway, the cation tetrahedra invert individually and sequentially.

Before further discussion, we define some terminology. By convention, we represent cation-centered tetrahedra here, but of course, an equivalent description could be constructed using anion-centered tetrahedra for these wurtzite-derived structures. A cation tetrahedron consists of one cation and its neighboring four anions. In the wurtzite structure (and wurtzite-type structures), one cation-anion bond in each tetrahedron has a notably different bond length from the other three, thus contributing to the spontaneous polarization and defining the polar axis of the structure; we continue this for individual tetrahedra, e.g., *c* direction for $MgSiN_2$ as shown in Fig. 4. The crystallographic axes are labeled according to the convention followed in Inorganic Crystal Structure Database structure files. In addition, we define the starting polarization direction as down and the opposite one as up. Viewing down the polarization axis, the remaining three anions form hexagonal patterns in a plane that we refer to as the hexagonal plane, again consistent with convention.

Structure 1 in Fig. 4 shows the starting positive-polarity structure in which all Mg and Si tetrahedra are pointing down along the *c* axis. Proceeding toward polarization inversion (analogous to applying an electric field opposing the spontaneous polarization of structure 1), the cations displace toward the hexagonal plane, increasing the bond length with the apical anion but decreasing the spontaneous polarization. Structure 2 shows the atomic structure associated with the first barrier to polarization inversion. At this point, one of the Si atoms has displaced fully to the hexagonal plane. As the switching continues, the Si cation emerges on the opposite side of the hexagonal plane, defining its affiliated tetrahedron in the up direction. A nearby Mg tetrahedron flips barrierlessly according to the decrease in energy from structure 2 to structure 3. The barrier between structures 3 and 4 is associated with another Si reaching the hexagonal plane, and again a nearby Mg tetrahedron flips barrierlessly from structure 4 to structure 5. Structure 5 shows the nonpolar intermediate structure in which half of the tetrahedra point up and the other half point down. We refer to such structures as half-switched (HS) in this paper as they have zero net polarization and represent the halfway point in the polarization inversion process.

The second half of the switching pathway, from nonpolar to negative polarity, is symmetric to the first half, such that the overall tetrahedra switching sequence for $MgSiN_2$ is Si-Mg-Si-Mg-Mg-Si-Mg-Si. Because this process proceeds via the distinct inversion of

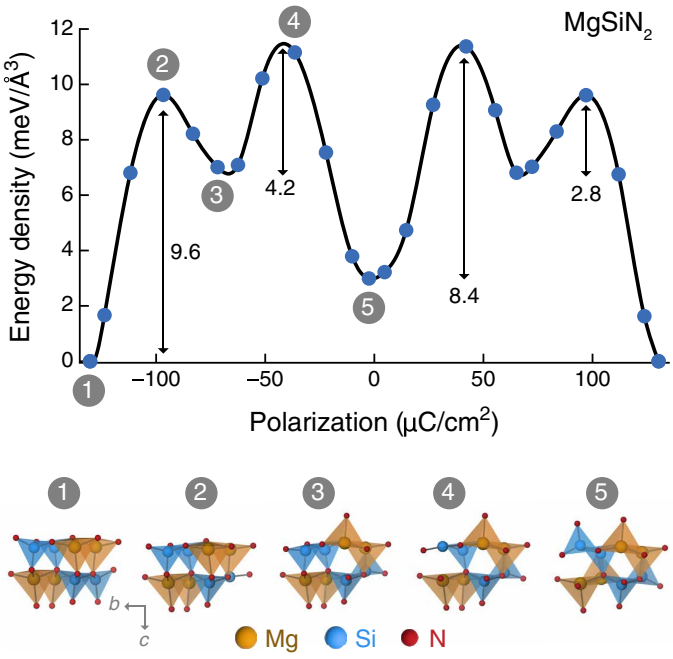

Fig. 4. Individual switching in multinary compounds. Polarization switching in $MgSiN_2$ proceeds via the individual mechanism. Structures (1) to (5) showcase only the first half of the switching pathway. Structure (1) represents the positive-polarity structure. Structures (2) to (5) are the intermediate structures along the switching pathway. Structure (5) is a unique half-switched, nonpolar structure. The crystallographic axes are such that the cation tetrahedra are pointed along the *c* axis.

individual tetrahedra rather than via the collective and simultaneous inversion described in Fig. 3, we refer to this as an individual switching pathway. All 22 candidates that share this feature of individual tetrahedra flipping are sequentially subjected to a systematic study on switching sequence; this analysis and the derived implication for design principles are discussed in the "Switching dominated by less electropositive cations" section.

In addition to differences in switching sequences, we also identify five unique HS nonpolar structures (see Fig. 5), including the β-BeO–like structure recently identified (*22*, *23*), among the 22 multinary compounds studied here. HS structures are key features of polarization switching pathways and they resemble the halfway milepost of the switching pathway. Figure 5 shows these structures with the polar *c* axis in the vertical direction, and we choose to view each *c* axis–containing plane along a direction such that no cation obscures the view of a cation of a different chemistry. All the five structures are available on GitHub: https://github.com/prashungorai/papers/tree/main/2023/polarization_switching_mechanism. A correlation exists between these HS structures and compound stoichiometry. There are five chemistry groups with different stoichiometries, namely, 1-1-2, 1-2-3, 2-1-3, 3-1-4, and 2-1-1-4, where the last number refers to the number of anions in the formula unit and the earlier numbers refer to distinct cation species.

Among 22 studied compounds, most compounds with 1-1-2 stoichiometry, of which $MgSiN_2$ is an example, exhibit the "NP1" nonpolar structure (Fig. 5A) as their intermediate HS structure along the switching pathway. We note that the NP1 structure is the β-BeO–like structure. The only exception is $LiAlS_2$, which has the NP2 structure. Figure 5 showcases the difference between NP1 and NP2, and we further highlight the repeating pattern of these five HS structures in fig. S1. For the 2-1-3 stoichiometry, most nitrides like Mg_2PN_3 have the NP3 HS structure while Zn_2PN_3 and oxides prefer the NP4 structure. We find that the NP3 structure is the cubanite (Fe_2CuS_3) structure type (*39*). All 1-2-3 nitrides have the NP4 structure. Last, compounds with 3-1-4 and 2-1-1-4 stoichiometries adopt the NP5 HS structure. In addition to the correlation between stoichiometry and nonpolar structures, there are correlations between the switching sequences of cation tetrahedra and the HS structures. To reach the nonpolar NP2 HS structure, $LiAlS_2$ have all the Li tetrahedra switched before the last Al tetrahedra is switched (Fig. 6). In comparison, the rest of the compounds with 1-1-2 stoichiometry have all the more-electronegative cation tetrahedra switched first, followed by the switching of tetrahedra of more-electropositive cations. Similar correlation between the switching sequence of cation tetrahedra and HS structures can also be seen for Mg_2PN_3 and Zn_2PN_3, which share similar chemistry and structure but have different switching sequences and HS structures.

Overall, among these 22 multinary compounds, we identify five unique HS structures, and most of them have not been reported in the context of wurtzite-type ferroelectrics, except for the NP1 β-BeO–like structure. While these five HS structures are by no means exhaustive, they offer a glimpse into the expected diversity of the nonpolar intermediate structures along the switching pathway of wurtzite-type multinary compounds. These HS structures provide insights into the inversion boundary between positive-polarity and negative-polarity domains for wurtzite-type materials with multinary chemistry.

Switching dominated by less electropositive cations

Our recent works (*12*, *14*) and results from other research groups (*8*, *10*) have challenged the idea of focusing on wurtzite *c*/*a* as a key indicator of switching barrier and, thus, a coercive field for wurtzite-type materials. Instead, we recently showed that local bond ionicity and bond strength are two promising knobs to engineer a wurtzite-type ferroelectric material (*12*, *14*). Using $Zn_{1-x}Mg_xO$ and $Al_{1-x}Sc_xN$ as examples, Mg (Sc) forms more ionic cation-anion bonds than Zn (Al) and, thus, reduces the coercive field. However, for the emerging wurtzite-type multinary candidates we recently identified (e.g., $MgSiN_2$, Mg_2PN_3, Li_2GeO_3, and Li_2GeO_3), how to effectively apply these two design principles remains unclear.

To address this question, we analyze the switching pathway for each of the 22 candidates that feature individual switching. We first extract the features of their pathways, including number of peaks, relative barrier heights, and the moving atoms and their electronegativities (χ) corresponding to each peak. Figure 6 compares these features for the 22 candidates ordered by their switching barriers with the largest at the top. Each individual cation tetrahedron has a corresponding circle whose area represents the relative energy barrier to invert the polarization of that tetrahedron, normalized by the largest barrier for each material. The barriers are calculated based on the tetrahedra switching sequence from left to right in the same manner as shown in Fig. 4. Open squares indicate barrierless tetrahedron inversion, and this only happens when multiple cation tetrahedra are associated with a peak, e.g., moving from structure 2 to 3 in Fig. 4. Last, colors show the relative χ of the cations of a multinary compound.

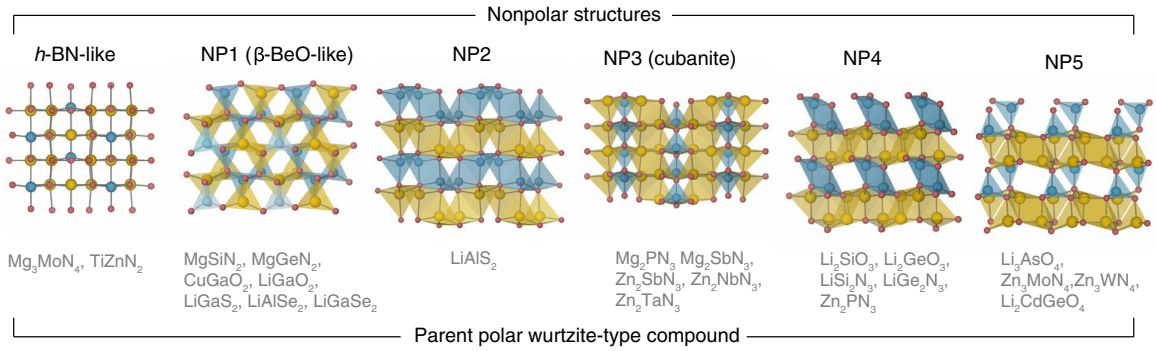

Fig. 5. Nonpolar, half-switched structures in multinary wurtzite-type compounds. Structures are named NP1 to NP5, with the parent polar wurtzite-type compounds listed below. Cations with higher and lower electronegativities are shown in blue and yellow, respectively. Red atoms are anions. The hexagonal BN–like nonpolar structure is shown for reference. NP1 is identical to the β-BeO–like structure previously reported (*22*), and NP3 is the cubanite structure (Fe_2CuS_3 type). (*39*)

Across all 22 multinary compounds, we find that the first barrier is always the highest one among all the peaks. The first barrier is also always associated with cations with high χ, and most of the major peaks are also associated with cations of high χ. Overall, this indicates that polarization switching barriers for these candidates are predominately determined by the highest χ cation and should be targeted to further decrease the switching barrier.

Using one of the top candidates from our previous search, $MgSiN_2$, as an example, our analysis shows that its switching barrier is associated with switching of Si-N tetrahedra. Therefore, the refined design principles suggest that alloying $MgSiN_2$ with same-valence cations to Si (same oxidation state) and lower in χ, e.g., Ti, Zr, and Hf, can be an effective route to further reduce its switching barrier. This design principle is also applicable to $Al_{1-x}Sc_xN$ alloys at compositions where it exhibits individual switching: Al, which has higher χ than Sc, is associated with the major peaks along the switching pathway and Al tetrahedra are the first to flip their polarity. This reinforces the importance of the local environment on polarization reversal in wurtzites, as increasing Sc content in $Al_{1-x}Sc_xN$ reduces E_c not because the Sc switches more easily, but because the presence of Sc-N bonds makes it easier for nearby Al tetrahedra to reverse polarity.

Last, among these multinary compounds, we find that those with higher switching barriers generally have fewer peaks than those with lower switching barriers (fig. S5). Using the family of II_2-IV-N_3 compounds as example, Zn_2PN_3, which has highest switching barrier, has only two peaks. Mg_2PN_3, which has second largest barrier, has four peaks. The rest, whose barriers are the lowest among all the studied compounds, have eight peaks. This suggests that a more complex energy landscape along the switching pathway can be expected to have a smaller barrier than one that switches collectively. Again, we observe the same behavior in $Al_{1-x}Sc_xN$ alloys where increasing Sc leads to more complex energy landscapes and progressively reduced switching barrier (Fig. 2D).

DISCUSSION

In summary, we perform a detailed study of the switching mechanisms for $Al_{1-x}Sc_xN$ alloys and multinary candidates from our recent computational search. We find that the commonly assumed wurtzite-hexagonal-wurtzite collective switching pathway found in binary wurtzite materials like AlN is not frequently observed in multinary compounds or in $Al_{1-x}Sc_xN$ alloys with high Sc composition ($x \gtrsim 0.22$). Instead, increasing chemical complexity seems to lead to different switching mechanisms, with cation tetrahedra switching individually. For the studied multinary wurtzite-type compounds that follow such an individual switching pathway, we identify five nonpolar HS structures that are different from layered hexagonal structures. This list of nonpolar structures is by no means exhaustive, and we expect to find more nonpolar structures in other multinary wurtzite-type compounds. Nonetheless, knowledge of these nonpolar structures provides the foundation for future investigation into domain motion and inversion boundaries.

For $Al_{1-x}Sc_xN$ alloys, we find that the polarization switching mechanism depends on Sc composition x and that higher x gives rise to lower switching barrier and promotes an individual switching pathway. Furthermore, for the same Sc composition, alloy models with individual switching pathways have lower switching barriers than the ones that follow a collective switching pathway. Last, we systematically examine the switching pathways for all the 22 compounds with individual switching and find that the largest barriers are associated with the motion of cations with high electronegativity. We also observed the same behavior in $Al_{1-x}Sc_xN$ alloys that exhibit individual switching. These findings give rise to a new design principle to lower switching barriers of multinary wurtzite-type materials—for the alloying approach, we need to focus on the cations with high χ to reduce the barrier.

Besides these findings, we recognize that our simulation can be limited by the simulation cell due to periodic boundary conditions and cation ordering in the supercells. However, in general, atomic motions in a smaller simulation cell tends to be more collective than the ones in a larger simulation cell. Therefore, we expect more "individual" switching behavior in larger supercells. We also acknowledge the known limitations (*11*, *31*, *32*) that the coercive fields derived from the SS-NEB switching pathway generally overestimate the experimental values because domain wall motion (*40*), defects, or field inhomogeneities are not considered (*41*, *42*). However, the agreement between our results and experimental trends for $Al_{1-x}Sc_xN$ alloys supports the assumption that SS-NEB calculations can qualitatively examine the required energy to switch polarization. Our current computational study is entirely focused on energetics of intermediate structures along switching pathways and therefore does not explicitly address the dynamics of the switching process. However, as demonstrated in the recent reports from Schönweger *et al.* and Calderon *et al.* (*21*, *23*), direct imaging of domain walls resulting

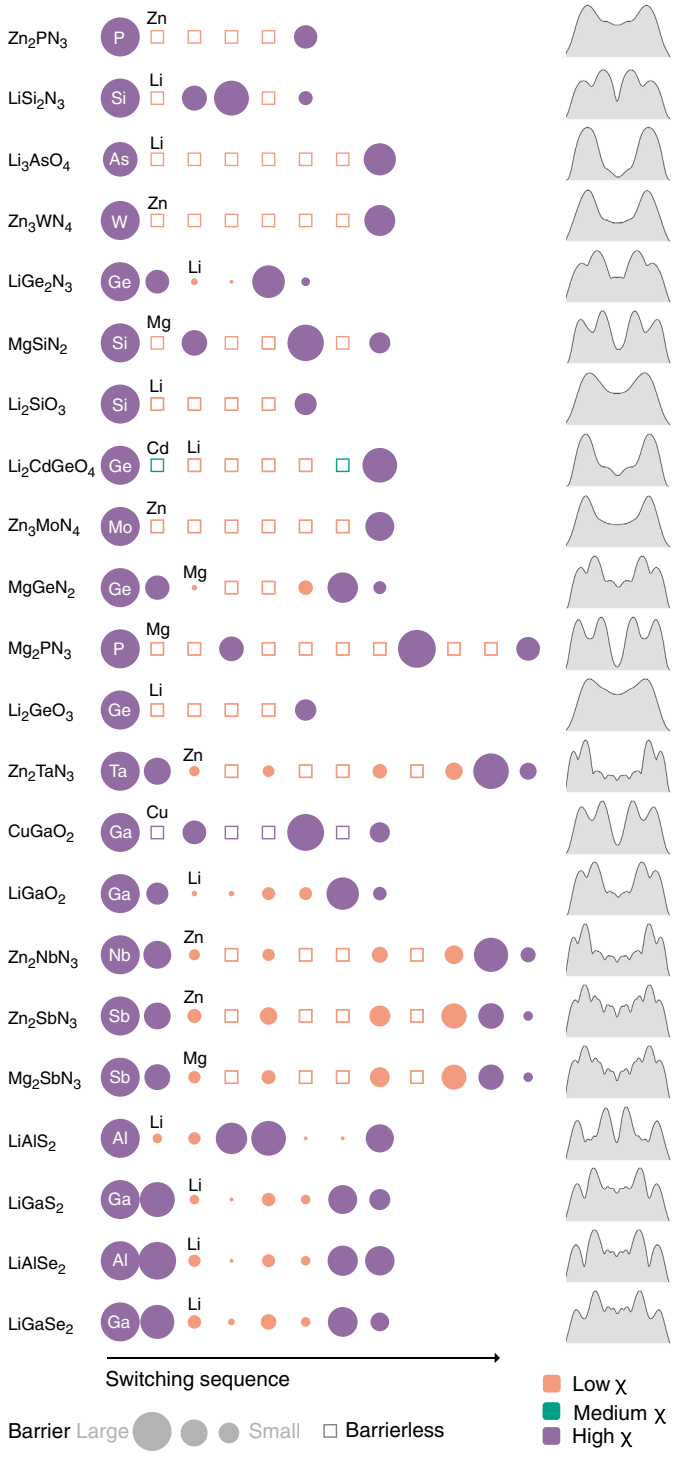

Fig. 6. Cation tetrahedra switching sequences. Each marker (circle and square) corresponds to inversion of a cation tetrahedron. Polarization switching pathways (similar to Figures 3 and 4) are shown as gray shaded areas. Circle areas scale with switching barrier, normalized to the largest value for each compound. Open squares indicate barrierless inversion. Colors denote the relative electronegativity (χ) of the cations.

from interrupted switching processes can provide important information about these intermediate structures.

MATERIALS AND METHODS

DFT calculation parameters

We used density functional theory (DFT) to calculate total energy and to perform structural relaxations. DFT calculations were performed using the plane-wave Vienna Ab-initio Simulation Package (VASP 5.4.4) (*43*) and the Perdew-Burke-Ernzerhof exchange correlation functional within the generalized gradient approximation (GGA) (*44*). The core electrons were treated with the projector-augmented wave method. For most transition metals (except Zn and Cd), we used the GGA + U approach with $U = 3.0$ eV on-site potential applied to the d orbitals. For Cu, we applied $U = 5.0$ eV to the d orbitals. The choice of U values follows the recipe in (*45*), which is known to provide better prediction of the formation enthalpy under standard conditions and, therefore, the thermodynamic stability of materials. The plane waves were expanded up to an energy cutoff of 340 eV and the Brillouin zone was sampled using automatically generated Γ-centered Monkhorst-Pack **k**-point grids with a length of 20. The structures are relaxed until the residual forces on each atom are below 0.01 eV/AA and total energy is converged to within 10^{-6} eV.

Polarization switching pathway and barrier

We applied the SS-NEB method (*46*) to determine the polarization switching pathways between the positive- and negative-polarity structures, and to calculate the energy barriers (ω_s) along the pathways. We generated initial images along the pathway via linear interpolation of positive- and negative-polarity structures. The SS-NEB method is distinct from NEB in that it allows relaxation of all degrees of freedom—cell volume and shape, and ion positions; NEB allows relaxation of ion positions only. Consequently, SS-NEB calculations are substantially more expensive than NEB. We performed SS-NEB calculations using the VASP Transition State Theory (VTST) tools developed by Henkelman *et al.* (*47*) as implemented in the vtst-182 code.

We found that converging SS-NEB calculations for materials exhibiting individual switching is generally challenging due to the complexity of their MEPs, i.e., the need to resolve multiple peaks instead of one or two peaks for the collective mechanism. We recommend the following procedure to converge SS-NEB calculations in these cases. First, the positive- and negative-polarity structures were fully relaxed with DFT. The interpolated images were then created using linear interpolation. In our experience, we found that the number of images need to be at least two to three times the number of cations in the simulation cell to converge the SS-NEB calculations and sufficiently resolve the peaks to calculate ω_s.

During the SS-NEB calculations, if one finds that the "distance" (along the configuration coordinate) increases drastically from one simulation iteration to the next, it is an indication that even more intermediate images are needed for convergence. When the total number of images became large (>96 images), we sliced the semi-converged pathways into segments using the local minima as slicing points. For each segment, we fully relaxed the local minima structure and used them as the end images to perform separate SS-NEB calculations. In the end, we patch the different segments to create the complete MEP without any issue. We highly recommend following this procedure if one hopes to converge these complex pathways.

Spontaneous polarization

We followed the modern theory of polarization, which uses the Berry phase approximation to calculate the electronic contribution to polarization. We used the implementation in VASP 5.4.4. to calculate the electronic contribution to polarization and chose (0.25, 0.25, 0.25) crystal coordinates as the center of the reference frame for dipole calculations. We used the atomic positions and assumed point charges to calculate the ionic contribution to polarization, as implemented in Pymatgen (*48*). We calculated the polarization from both the MEP determined by SS-NEB and linear-interpolated pathway between the positive- and negative-polarity structures. We found that the spontaneous polarization values from these two different pathways are equal for all the studied compounds and alloys. As an example, fig. S2 shows the comparison between the two approaches for Mg_2PN_3. This suggests that, despite the individual switching, spontaneous polarization itself is consistent whether the accurate MEP determined by SS-NEB or the simple linear-interpolated pathway (which inevitably results in the hexagonal phase as the nonpolar structure) is considered.

Switching pathway and barrier for alloys

The computational workflow for calculating the average switching barrier (ω_s) and spontaneous polarization (P_s) of $Al_{1-x}Sc_xN$ alloys is schematically shown in fig. S3. To sample the different local environments in an alloy, we created four different structural models at each composition (x) by randomly distributing Al and Sc on the cation sublattice of a 72-atom AlN supercell. We chose four structures to generate statistics of ω_s and P_s while keeping the computational cost manageable for MEPs of individual switching. Additionally, statistical sampling is important because it helps us resolve the transition regime where it is a mix of collective and individual mechanisms. Alloy modeling with other methods such as special quasirandom structures (SQS) will not allow such statistical sampling because it generates a single structural model. The alloy structures were fully relaxed with DFT. We then performed SS-NEB without any additional constraints (e.g., strain) on the simulation cells and pathways to determine the lowest energy switching pathway and calculate ω_s, and used the modern theory of polarization to calculate P_s. Finally, we averaged ω_s and P_s across the four structures at each x.

Supplementary Materials

This PDF file includes:

Figs. S1 to S5

REFERENCES AND NOTES

1. D. Ielmini, H.-S. P. Wong, In-memory computing with resistive switching devices. *Nat. Electron.* **1**, 333–343 (2018).
2. T. Y. Kim, S. K. Kim, S.-W. Kim, Application of ferroelectric materials for improving output power of energy harvesters. *Nano Converg.* **5**, 30 (2018).
3. T. Mikolajick, S. Slesazeck, H. Mulaosmanovic, M. H. Park, S. Fichtner, P. D. Lomenzo, M. Hoffmann, U. Schroeder, Next generation ferroelectric materials for semiconductor process integration and their applications. *J. Appl. Phys.* **129**, 100901 (2021).
4. S. Fichtner, N. Wolff, F. Lofink, L. Kienle, B. Wagner, AlScN: A III-V semiconductor based ferroelectric. *J. Appl. Phys.* **125**, 114103 (2019).
5. C. E. Dreyer, A. Janotti, C. G. Van de Walle, D. Vanderbilt, Correct implementation of polarization constants in wurtzite materials and impact on III-nitrides. *Phys. Rev. X* **6**, 021038 (2016).
6. K.-H. Kim, I. Karpov, R. H. Olsson III, D. Jariwala, Wurtzite and fluorite ferroelectric materials for electronic memory. *Nat. Nanotechnol.* **18**, 422–441 (2023).
7. D. Wang, P. Wang, B. Wang, Z. Mi, Fully epitaxial ferroelectric ScGaN grown on GaN by molecular beam epitaxy. *Appl. Phys. Lett.* **119**, 111902 (2021).
8. J. Hayden, M. D. Hossain, Y. Xiong, K. Ferri, W. Zhu, M. V. Imperatore, N. Giebink, S. Trolier-McKinstry, I. Dabo, J.-P. Maria, Ferroelectricity in boron-substituted aluminum nitride thin films. *Phys. Rev. Mater.* **5**, 044412 (2021).
9. D. Wang, S. Mondal, J. Liu, M. Hu, P. Wang, S. Yang, D. Wang, Y. Xiao, Y. Wu, T. Ma, Z. Mi, Ferroelectric YAlN grown by molecular beam epitaxy. *Appl. Phys. Lett.* **123**, 033504 (2023).
10. K. Ferri, S. Bachu, W. Zhu, M. Imperatore, J. Hayden, N. Alem, N. Giebink, S. Trolier-McKinstry, J.-P. Maria, Ferroelectrics everywhere: Ferroelectricity in magnesium substituted zinc oxide thin films. *J. Appl. Phys.* **130**, 044101 (2021).
11. H. Moriwake, R. Yokoi, A. Taguchi, T. Ogawa, C. A. J. Fisher, A. Kuwabara, Y. Sato, T. Shimizu, Y. Hamasaki, H. Takashima, M. Itoh, A computational search for wurtzite-structured ferroelectrics with low coercive voltages. *APL Mater.* **8**, 121102 (2020).
12. K. Yazawa, J. S. Mangum, P. Gorai, G. L. Brennecka, A. Zakutayev, Local chemical origin of ferroelectric behavior in wurtzite nitrides. *J. Mater. Chem. C* **10**, 17557–17566 (2022).
13. Y. Dai, M. Wu, Covalent-like bondings and abnormal formation of ferroelectric structures in binary ionic salts. *Sci. Adv.* **9**, eadf8706 (2023).
14. C.-W. Lee, N. U. Din, K. Yazawa, G. L. Brennecka, A. Zakutayev, P. Gorai, Emerging materials and design principles for wurtzite-type ferroelectrics. ChemRxiv (2023). 10.26434/chemrxiv-2023-hf60w.
15. A. Konishi, T. Ogawa, C. A. J. Fisher, A. Kuwabara, T. Shimizu, S. Yasui, M. Itoh, H. Moriwake, Mechanism of polarization switching in wurtzite-structured zinc oxide thin films. *Appl. Phys. Lett.* **109**, 102903 (2016).
16. F. Bernardini, V. Fiorentini, D. Vanderbilt, Spontaneous polarization and piezoelectric constants of III-V nitrides. *Phys. Rev. B* **56**, R10024–R10027 (1997).
17. M. B. Geilikman, Mechanisms of polytype stabilization during the wurtzite-sphalerite transition. *Phys. Chem. Miner.* **8**, 2–7 (1982).
18. L. T. Romano, J. E. Northrup, M. A. O'Keefe, Inversion domains in GaN grown on sapphire. *Appl. Phys. Lett.* **69**, 2394–2396 (1996).
19. N. Stolyarchuk, T. Markurt, A. Courville, K. March, J. Zúñiga-Pérez, P. Vennéguès, M. Albrecht, Intentional polarity conversion of AlN epitaxial layers by oxygen. *Sci. Rep.* **8**, 14111 (2018).
20. T. Akiyma, M. Uchino, K. Nakamura, T. Ito, S. Xiao, H. Miyake, Structural analysis of polarity inversion boundary in sputtered AlN films annealed under high temperatures. *Jpn. J. Appl. Phys.* **58**, SCCB30 (2019).
21. G. Schönweger, N. Wolff, M. R. Islam, M. Gremmel, A. Petraru, L. Kienle, H. Kohlstedt, S. Fichtner, In-grain ferroelectric switching in sub-5 nm thin $Al_{0.74}Sc_{0.26}N$ films at 1 V. *Adv. Sci.* **10**, 2302296 (2023).
22. Z. Liu, X. Wang, X. Ma, Y. Yang, D. Wu, Doping effects on the ferroelectric properties of wurtzite nitrides. *Appl. Phys. Lett.* **122**, 122901 (2023).
23. S. Calderon V, J. Hayden, S. M. Baksa, W. Tzou, S. Trolier-McKinstry, I. Dabo, J.-P. Maria, E. C. Dickey, Atomic-scale polarization switching in wurtzite ferroelectrics. *Science* **380**, 1034–1038 (2023).
24. M. Akiyama, T. Kamohara, K. Kano, A. Teshigahara, Y. Takeuchi, N. Kawahara, Enhancement of piezoelectric response in scandium aluminum nitride alloy thin films prepared by dual reactive cosputtering. *Adv. Mater.* **21**, 593–596 (2009).
25. F. Tasnádi, B. Alling, C. Höglund, G. Wingqvist, J. Birch, L. Hultman, I. A. Abrikosov, Origin of the anomalous piezoelectric response in wurtzite $Sc_xAl_{1-x}N$ alloys. *Phys. Rev. Lett.* **104**, 137601 (2010).
26. S. Zhang, D. Holec, W. Y. Fu, C. J. Humphreys, M. A. Moram, Tunable optoelectronic and ferroelectric properties in Sc-based III-nitrides. *J. Appl. Phys.* **114**, 133510 (2013).
27. K. Yazawa, A. Zakutayev, G. L. Brennecka, A Landau–Devonshire analysis of strain effects on ferroelectric $Al_{1-x}Sc_xN$. *Appl. Phys. Lett.* **121**, 042902 (2022).
28. M. E. Lines, A. M. Glass, *Principles and Applications of Ferroelectrics and Related Materials* (Oxford Univ. Press, 2001).
29. S. Yasuoka, T. Shimizu, A. Tateyama, M. Uehara, H. Yamada, M. Akiyama, Y. Hiranaga, Y. Cho, H. Funakubo, Effects of deposition conditions on the ferroelectric properties of $(Al_{1-x}Sc_x)N$ thin films. *J. Appl. Phys.* **128**, 114103 (2020).
30. S. Rassay, F. Hakim, C. Li, C. Forgey, N. Choudhary, R. Tabrizian, A segmented-target sputtering process for growth of sub-50 nm ferroelectric scandium-aluminum-nitride films with composition and stress tuning. *Phys. Status Solidi Rapid Res. Lett.* **15**, 2100087 (2021).
31. H. Wang, N. Adamski, S. Mu, C. G. Van de Walle, Piezoelectric effect and polarization switching in $Al_{1-x}Sc_xN$. *J. Appl. Phys.* **130**, 104101 (2021).
32. M. Kruse, U. Petralanda, M. N. Gjerding, K. W. Jacobsen, K. S. Thygesen, T. Olsen, Two-dimensional ferroelectrics from high throughput computational screening. *npj Comput. Mater.* **9**, 45 (2023).
33. R. Resta, Macroscopic polarization in crystalline dielectrics: The geometric phase approach. *Rev. Mod. Phys.* **66**, 899–915 (1994).
34. N. Takeuchi, First-principles calculations of the ground-state properties and stability of ScN. *Phys. Rev. B* **65**, 045204 (2002).
35. H. Moriwake, A. Konishi, T. Ogawa, K. Fujimura, C. A. Fisher, A. Kuwabara, T. Shimizu, S. Yasui, M. Itoh, Ferroelectricity in wurtzite structure simple chalcogenide. *Appl. Phys. Lett.* **104**, 242909 (2014).

36. J. Breternitz, S. Schorr, Symmetry relations in wurtzite nitrides and oxide nitrides and the curious case of $Pmc2_1$. *Acta Crystallogr. A Found. Adv* **77**, 208–216 (2021).
37. R. Woods-Robinson, V. Stevanović, S. Lany, K. N. Heinselman, M. K. Horton, K. A. Persson, A. Zakutayev, Role of disorder in the synthesis of metastable zinc zirconium nitrides. *Phys. Rev. Mater.* **6**, 043804 (2022).
38. C. L. Rom, R. W. Smaha, C. A. Knebel, K. N. Heinselman, J. R. Neilson, S. R. Bauers, A. Zakutayev, Bulk and film synthesis pathways to ternary magnesium tungsten nitrides. *J. Mater. Chem. C* **11**, 11451–11459 (2023).
39. C. McCammon, J. Zhang, R. M. Hazen, L. W. Finger, High-pressure crystal chemistry of cubanite, $CuFe_2S_3$. *Am. Mineral.* **77**, 937–944 (1992).
40. H. Mulaosmanovic, E. Chicca, M. Bertele, T. Mikolajick, S. Slesazeck, Mimicking biological neurons with a nanoscale ferroelectric transistor. *Nanoscale* **10**, 21755–21763 (2018).
41. A. K. Tagantsev, I. Stolichnov, N. Setter, J. S. Cross, M. Tsukada, Non-Kolmogorov-Avrami switching kinetics in ferroelectric thin films. *Phys. Rev. B* **66**, 214109 (2002).
42. S. Zhukov, Y. A. Genenko, O. Hirsch, J. Glaum, T. Granzow, H. von Seggern, Dynamics of polarization reversal in virgin and fatigued ferroelectric ceramics by inhomogeneous field mechanism. *Phys. Rev. B* **82**, 014109 (2010).
43. G. Kresse, J. Furthmüller, Efficient iterative schemes for ab initio total-energy calculations using a plane-wave basis set. *Phys. Rev. B* **54**, 11169–11186 (1996).
44. J. P. Perdew, K. Burke, M. Ernzerhof, Generalized gradient approximation made simple. *Phys. Rev. Lett.* **77**, 3865–3868 (1996).
45. V. Stevanović, S. Lany, X. Zhang, A. Zunger, Correcting density functional theory for accurate predictions of compound enthalpies of formation: Fitted elemental-phase reference energies. *Phys. Rev. B* **85**, 115104 (2012).
46. D. Sheppard, P. Xiao, W. Chemelewski, D. D. Johnson, G. Henkelman, A generalized solid-state nudged elastic band method. *J. Chem. Phys.* **136**, 074103 (2012).
47. G. Henkelman, B. P. Uberuaga, H. Jónsson, A climbing image nudged elastic band method for finding saddle points and minimum energy paths. *J. Chem. Phys.* **113**, 9901–9904 (2000).
48. T. E. Smidt, S. A. Mack, S. E. Reyes-Lillo, A. Jain, J. B. Neaton, An automatically curated first-principles database of ferroelectrics. *Sci. Data* **7**, 72 (2020).

Acknowledgments

Funding: Support for this work was provided by the National Science Foundation under grant no. DMR-2119281 at the Colorado School of Mines and by the Office of Science (SC), Office of Basic Energy Sciences (BES) as part of an Early Career Award at the National Renewable Energy Laboratory, operated by the Alliance for Sustainable Energy LLC, for the U.S. Department of Energy (DOE) under contract no. DE-AC36-08GO28308. The work (energy calculations to understand switching mechanism) was also partially supported by DOE BES, with additional support from Advanced Scientific Computing Research (ASCR), under program ERW6548. The research was performed using computational resources sponsored by DOE's Office of Energy Efficiency and Renewable Energy and located at the NREL. The views expressed in the article do not necessarily represent the views of the DOE or the U.S. Government. **Author contributions:** C-W. L.: Conceptualization, investigation, methodology, data curation, validation, formal analysis, visualization, writing—original draft, and writing—review and editing. K.Y.: Investigation and writing—review and editing. A.Z.: Conceptualization, writing—review and editing, funding acquisition, and supervision. G.L.B.: Conceptualization, writing—review and editing, project administration, funding acquisition, and supervision. P.G.: Conceptualization, investigation, methodology, data curation, validation, software, formal analysis, visualization, writing—original draft, writing—review and editing, supervision, project administration, and funding acquisition. **Competing interests:** The authors declare that they have no competing interests. **Data and materials availability:** All data needed to evaluate the conclusions in the paper are present in the paper and/or the Supplementary Materials.

Submitted 27 September 2023
Accepted 12 April 2024
Published 17 May 2024
10.1126/sciadv.adl0848